Response of Humidity and Clouds to Tropical Deep Convection

MARK D. ZELINKA AND DENNIS L. HARTMANN

Department of Atmospheric Sciences, University of Washington, Seattle, Washington

(Manuscript received 30 January 2008, in final form 14 August 2008)

ABSTRACT

Currently available satellite data can be used to track the response of clouds and humidity to intense precipitation events. A compositing technique centered in space and time on locations experiencing high rain rates is used to detail the characteristic evolution of several quantities measured from a suite of satellite instruments. Intense precipitation events in the convective tropics are preceded by an increase in low-level humidity. Optically thick cold clouds accompany the precipitation burst, which is followed by the development of spreading upper-level anvil clouds and an increase in upper-tropospheric humidity over a broader region than that occupied by the precipitation anomalies. The temporal separation between the convective event and the development of anvil clouds is about 3 h. The humidity increase at upper levels and the associated decrease in clear-sky longwave emission persist for many hours after the convective event. Large-scale vertical motions from reanalysis show a coherent evolution associated with precipitation events identified in an independent dataset: precipitation events begin with stronger upward motion anomalies in the lower troposphere, which then evolve toward stronger upward motion anomalies in the upper troposphere, in conjunction with the development of anvil clouds. Greater upper-tropospheric moistening and cloudiness are associated with larger-scale and better-organized convective systems, but even weaker, more isolated systems produce sustained upper-level humidity and clear-sky outgoing longwave radiation anomalies.

1. Introduction

Deep convective systems are prominent features of the tropical atmosphere that have important roles at a spectrum of space and time scales from local diurnal cycles to the planetary-scale Hadley and Walker circulations. Upward motion occurring in the ascending branches of the Hadley and Walker circulations is realized not in the form of large-scale continuous ascent, but in the form of a large number of relatively small-scale discrete convective plumes occurring in an otherwise subsiding environment (Yanai et al. 1973). Because it is the ensemble of transient deep convective processes that results in the measured mean ascent in the tropics, understanding the large-spatial-scale and long-temporal-scale tropical circulation requires understanding deep convective processes.

In addition to its dynamical importance for the tropical circulation, deep convection is the primary source of high clouds and free-tropospheric water vapor, which strongly impact the radiation budget of the planet. Stratiform anvil clouds characterized by negative net radiative forcing, and thin cirrus clouds characterized by positive net radiative forcing (Hartmann et al. 2001), spread outward from deep cumulonimbus clouds and are the most prominent clouds in the convective regions of the tropics. Moist boundary layer air is transported by deep convection to the dry mid- and upper troposphere, where even slight humidity increases can strongly reduce the radiation emitted to space (Shine and Sinha 1991; Udelhofen and Hartmann 1995; Spencer and Braswell 1997; Allan et al. 1999; Held and Soden 2000; Colman 2001). Indeed, Soden and Fu (1995) find that the frequency of deep convection is strongly correlated with changes in upper-tropospheric humidity, and that these variations are responsible for about half of the regional greenhouse effect variations. Because the ability of the tropics to retain heat determines how much energy is available for export to the rest of the earth (Pierrehumbert 1995), perturbations to the cloud and humidity fields in association with tropical deep convection strongly affect not only the local radiation budget, but also the energy budget of the entire planet.

The ability to properly simulate deep convection and the corresponding cloud and humidity fields remains a

Corresponding author address: Mark D. Zelinka, Department of Atmospheric Sciences, University of Washington, Box 351640, Seattle, WA 98195.
E-mail: mzelinka@atmos.washington.edu

DOI: 10.1175/2008JCLI2452.1

challenge to global climate models. Understanding how clouds and humidity will change under greenhouse warming is largely dependent on understanding the convective processes that determine their distribution, and this requires detailed measurements of tropical convective systems. In this study we use profiles of humidity retrieved by the Atmospheric Infrared Sounder (AIRS) and cloud properties from the Moderate Resolution Imaging Spectroradiometer (MODIS) on board the National Aeronautics and Space Administration's (NASA's) *Aqua* satellite to investigate the evolution of high clouds, humidity, and clear-sky outgoing longwave radiation (OLR_{CS}) associated with deep convection. The spatial and temporal humidity and cloud distributions are investigated by compositing about locations of deep convection, identified by intense rain rates (RRs) from the Tropical Rainfall Measuring Mission (TRMM) Multisatellite Precipitation Analysis (TMPA). In addition, we assess the sensitivity of the upper-tropospheric moisture and cloud evolution to the scale of the convection.

It is well known that while some tropical deep convection ''pops up'' in regions that are distant from synoptic support, the vast majority of deep convection is organized into convective complexes, which have been extensively documented (e.g., Houze and Betts 1981; Gamache and Houze 1983; Houze 1982; Chen and Houze 1997; Nuret and Chong 1998; Sherwood and Wahrlich 1999). These studies have largely relied on ground-based and geostationary satellite observations of individual convective systems during field campaigns. The present study aims to further detail the evolution of the moisture and cloud fields in the vicinity of tropical deep convective events throughout the tropical Pacific. We take a statistical approach as a means of showing climatological characteristics of convective systems rather than highly detailed observations of individual systems.

The AIRS instrument is uniquely suited for measuring the humidity distribution: It provides radiosonde-quality humidity and temperature retrievals at high vertical resolution throughout the troposphere, unlike geostationary water vapor channels, which sense vapor in a thick upper-tropospheric layer; its global coverage allows observations from a broader range of locations than those within the radiosonde network or within field campaign domains; the duration of observations allow for a larger and more diverse set of samples than those of field campaigns; and the cloud-clearing techniques employed in the AIRS retrieval algorithm (Susskind et al. 2003) allow for sampling with greater confidence in cloudy regions where infrared retrievals from other instruments become contaminated.

2. Data and quality control

We focus on the tropical Pacific ITCZ region (5°–15°N, 120°–260°E) between January 2003 and December 2005 using data from three sensors on board the *Aqua* satellite: AIRS, MODIS, and Advanced Microwave Scanning Radiometer for Earth Observing System (EOS; AMSR-E). We also use a precipitation dataset (TMPA) that includes measurements from a suite of polar-orbiting and geostationary satellites. Finally, we make use of vertical velocities from the National Centers for Environmental Prediction–National Center for Atmospheric Research (NCEP–NCAR) reanalysis. We reprocess all data to a 1° grid, keeping a record of number of samples within each grid space.

a. AIRS

AIRS is actually a suite of instruments—a hyperspectral infrared instrument (i.e., AIRS), with 2378 channels between 3.7 and 15.4 μm and a 13.5-km footprint at nadir; the Advanced Microwave Sounding Unit (AMSU)-A, with 15 microwave channels between 23 and 90 GHz and a 40.5-km footprint at nadir; and a visible/near-IR sensor with four channels between 0.40 and 0.94 μm and a 2.3-km footprint at nadir (Aumann et al. 2003). Within each AMSU-A field of view (FOV) there is an array of 3×3 AIRS FOVs, and within each AIRS FOV is an array of 8×9 visible/near-IR FOVs. The visible/near-IR channels are primarily used to flag the presence of low clouds (Gautier et al. 2003). Because information from all sensors is used simultaneously, the geophysical (level 2) retrievals are reported at the nominal resolution of 40.5 km at nadir.

The AIRS retrieval algorithm makes use of a cloud-clearing technique that takes advantage of the fact that while IR retrievals are strongly affected by the presence of clouds, microwave temperature retrievals are largely insensitive to the presence of clouds (Susskind et al. 2003). Thus, any horizontal inhomogeneity in the radiances observed by the 3×3 array of IR footprints within the microwave footprint is largely caused by varying amounts of clouds within each IR FOV. One important assumption in this approach is that only the relative amount, and not the radiative properties, of a given cloud type vary between the IR FOVs. A second assumption is that the geophysical properties that are retrieved in the clear portions of the FOVs are identical in each IR FOV. Making use of this technique neither requires a priori assumptions about or modeling of the cloud properties (height, emissivity, etc.), nor does it limit the IR retrievals to rare clear-sky scenes.

We use retrievals of OLR_{CS} and profiles of water vapor mixing ratio (w), saturation water vapor mixing

ratio (w_s), and temperature (T) from the AIRS version 4, level 2 (swath) product. The profile of w is a layer quantity, representing the mean mixing ratio between the standard pressure levels, while profiles of w_s and T are level quantities, representing the value at the pressure level. For temperatures higher than 273.15 K, w_s is calculated with respect to water; otherwise, it is calculated with respect to ice using the Buck (1981) formulation. We calculate the layer geometric mean w_s such that the calculated RH is a layer mean RH between pressure levels. AIRS version 4 OLR_{CS} retrievals are biased relative to the Clouds and the Earth's Radiant Energy System (CERES) by +8 to +10 W m^{-2} (S.-Y. Lee 2008, personal communication); however, we focus here on OLR_{CS} anomalies rather than absolute values, and so interpretation is not adversely affected by systematic bias.

Atmospheric T retrievals have been compared with European Centre for Medium-Range Weather Forecasts (ECMWF) analyses and dedicated radiosondes and are found to be accurate to 1°C for every 1-km-thick layer (Fetzer et al. 2005). Similarly, w profiles have been compiled in 2-km layers and compared with dedicated radiosondes. At the tropical west Pacific (TWP) site, Fetzer et al. (2005) found the following biases relative to radiosondes: −10.5% (1013–700 hPa), −0.7% (700–500 hPa), −2.3% (500–300 hPa), −16.1% (300–200 hPa), and 15.1% (200–150 hPa).

We apply all of the appropriate quality assurance flags (Susskind et al. 2006) to the AIRS dataset. Generally, precipitation and/or cloud fractions exceeding 80% in the AIRS fields of view cause the retrieval to fail. We perform additional quality control by removing all retrievals in which the RH with respect to liquid water [calculated using the Buck (1981) w_s formulation] exceeds 100% at any layer within the retrieval. This removes spuriously high RHs while allowing for humidities that are supersaturated with respect to ice, as is frequently observed in the upper troposphere (cf. Gettelman et al. 2006). Approximately 7% of the AIRS retrievals were removed because of supersaturation with respect to liquid water.

b. MODIS

The MODIS is a whiskbroom-scanning radiometer with 36 channels between 0.415 and 14.235 μm. As many as 20 channels are used in the cloud-detection algorithm to create a cloud mask at 1-km resolution, which is essentially a measure of the confidence that the FOV is clear (Platnick et al. 2003). CO_2 slicing within the broad 15-μm absorption band is then used to infer cloud-top pressure and the effective cloud amount on a 5×5 pixel (5 km at nadir) scene, assuming at least 4 of the 25 pixels are flagged as either probably cloudy or cloudy. Temperature profiles from the Global Data Assimilation System (GDAS) gridded meteorological product (Derber et al. 1991) are then used to derive cloud-top temperature (CTT). Optical thickness (τ) retrievals, which make use of the 0.65-, 0.86-, and 1.2-μm bands in addition to inferences about cloud phase, are only provided for the daytime observations (ascending orbits in the tropics). We remove cloud retrievals that are affected by sun glint and are over land, and those where the cloud mask is undetermined.

Cloud fraction, CTT, and τ are reported at 5-km resolution in the level 2 MODIS joint product, and we calculate histograms of average high (CTT $<$ 245 K) cloud fractions in three optical depth bins in 1° grid spaces as in Kubar et al. (2007). For each 1° grid space, we bin the cloud fractions based on τ ranges that are chosen to distinguish between high clouds with negative radiative forcing ($\tau \geq 4$) and high, thin clouds with positive radiative forcing ($\tau < 4$). The clouds with negative forcing are further separated into anvil ($4 \geq \tau < 32$) and thick ($\tau \geq 32$) clouds. The assumption here, which will be supported by the results, is that the intermediate optical depth cold cloud corresponds to extended upper-level anvil cloud associated with convection, while the thick, cold cloud is more closely associated with heavy precipitation.

c. AMSR-E

AMSR-E is a conically scanning passive microwave radiometer sensing polarized radiation at six frequencies between 6.9 and 89 GHz. The AMSR-E instrument and retrieval algorithms are explained in detail in Japan Aerospace Exploration Agency (2005). We use retrievals of column-integrated water vapor (WVP) over the ocean from the AMSR-E version 5 ocean product. WVP is retrieved using the 18.7-, 23.8-, and 36.5-GHz brightness temperatures. First, cloud liquid water index (CWI) is derived from brightness temperature, atmospheric transmittance, and vertical mean atmospheric temperature at 18.7 and 36.5 GHz. Then, WVP is calculated from the CWI, atmospheric transmittance at 18.7 and 23.8 GHz, and a set of regression coefficients that minimize differences between WVP and the precipitable water from radiosondes. These data are discarded in the presence of heavy rain.

d. TMPA

TMPA provides precipitation rates at 3-h resolution between 50°S and 50°N from a suite of polar-orbiting and geostationary satellites (Huffman et al. 2007). The data are collected from the Microwave Imager on TRMM, the Special Sensor Microwave Imager on the

Defense Meteorological Satellite Program satellites, AMSR-E on *Aqua*, and the Advanced Microwave Sounding Unit-B on the National Oceanic and Atmospheric Administration (NOAA) satellite series. These polar-orbiting passive microwave sensors cover about 80% of the earth's surface between 50°S and 50°N over 3-h periods. Precipitation data for the remaining 20% is inferred from window channel IR data collected by geostationary satellites. Three additional data sources are the TRMM Combined Instrument estimate, the Global Precipitation Climatology Project monthly rain gauge analysis, and the Climate Assessment and Monitoring System monthly rain gauge analyses.

Briefly, the TMPA RR estimates are made using the following procedure: the microwave estimates are calibrated and combined, IR estimates are created using the calibrated microwave precipitation, the microwave and IR estimates are combined, and, finally, the rain gauge data are incorporated as a means of scaling the retrieved precipitation estimates. We make use of the version 6 3B42 product reported at the nominal 3-hourly observation times (0000, 0300, . . . , 2100 UTC), which averages polar-orbiting data that are ±90 min from these times.

e. NCEP–NCAR reanalysis

Finally, 6-hourly horizontal and vertical winds from the NCEP–NCAR reanalysis (Kalnay et al. 1996) over the same period are used. These data are linearly interpolated from 2.5° to 1° horizontal resolution and to 3-hourly resolution.

3. Methodology

We are interested in the response to humidity and clouds to tropical deep convection from a statistical and climatological perspective rather than from a case-by-case perspective; thus, we composite the many thousands of deep convective events in the Pacific ITCZ over the 3-yr period of January 2003–December 2005. We locate deep convection by seeking RRs that exceed the 90th percentile, which, after gridding the data to 1° resolution, is 1.6 mm h^{-1} for this time period in the tropical Pacific (from −25° to 25°N, 120°–260°E). During the 3-yr period of study, 57% of total rainfall in the tropical Pacific fell in RR events that exceeded the 90th percentile. Thus, by choosing the 90th percentile of RR as a threshold, we concentrate on the very intense convection that makes up a substantial portion of the total accumulated precipitation while still retaining a large sample size.

We composite the meteorological fields in 11 × 11 grids of 1° grid spaces surrounding each RR grid space exceeding this threshold value and for the 24 h before and 24 h after the time of deep convection. Where multiple adjacent grid spaces exceed the RR threshold, the composites centered at each rainy grid space are averaged into one distinct realization to maintain the most conservative estimate of the number of independent samples.

Even though *Aqua* passes over a given location only once every 12 h in the tropics, the precipitation data are provided every 3 h everywhere, thereby resulting in a sampling of geophysical quantities at a wide range of time offsets from the deep convection events. We choose composite temporal increments of 3 h by averaging all retrievals that fall within ±90 min of the 3-h increments. For example, any *Aqua* overpass that occurred between 4.5 and 1.5 h prior to a high RR observation is placed at hour −3.

The use of a reference frame centered on intense RRs, which is fixed in time over the 48-h period surrounding the convective events, is chosen to study the effects of convection on the environment in an Eulerian sense. Unlike the studies of Soden (1998, 2004) and Sherwood and Wahrlich (1999), we do not attempt to track convective systems, but rather concentrate on the effects of convection on the environment through which the convection passes. Thus, we sample a spectrum of convection from events that pop up stochastically to convective systems that propagate through the domain in time.

Composite anomalies are computed by subtracting the temporal mean of the composite mean pattern over the 48-h period from each time lag. As will be shown below, many anomalies propagate out of the domain, so it is not always possible to say with certainty when they have spread to their largest extent or have reached their maximum amplitudes. In these cases, we simply put a lower bound on the time at which these occur.

4. Results

Results are shown for convection observed within the tropical Pacific ITCZ, defined as 5°–15°N, 120°–260°E. Aside from spatial pattern differences resulting from underlying SSTs, the results shown here are robust throughout the tropics, assuming a climatologically convective region is chosen for analysis. Composites generated using only observations from ascending *Aqua* passes (1330 LST) show no differences from those generated using only descending *Aqua* passes (0130 LST); seasonal differences also do not affect the results.

a. Composites about all RRs exceeding the 90th percentile

Plan views of six composite mean variables as a function of time relative to the high-precipitation event are shown in Fig. 1. As required by the compositing

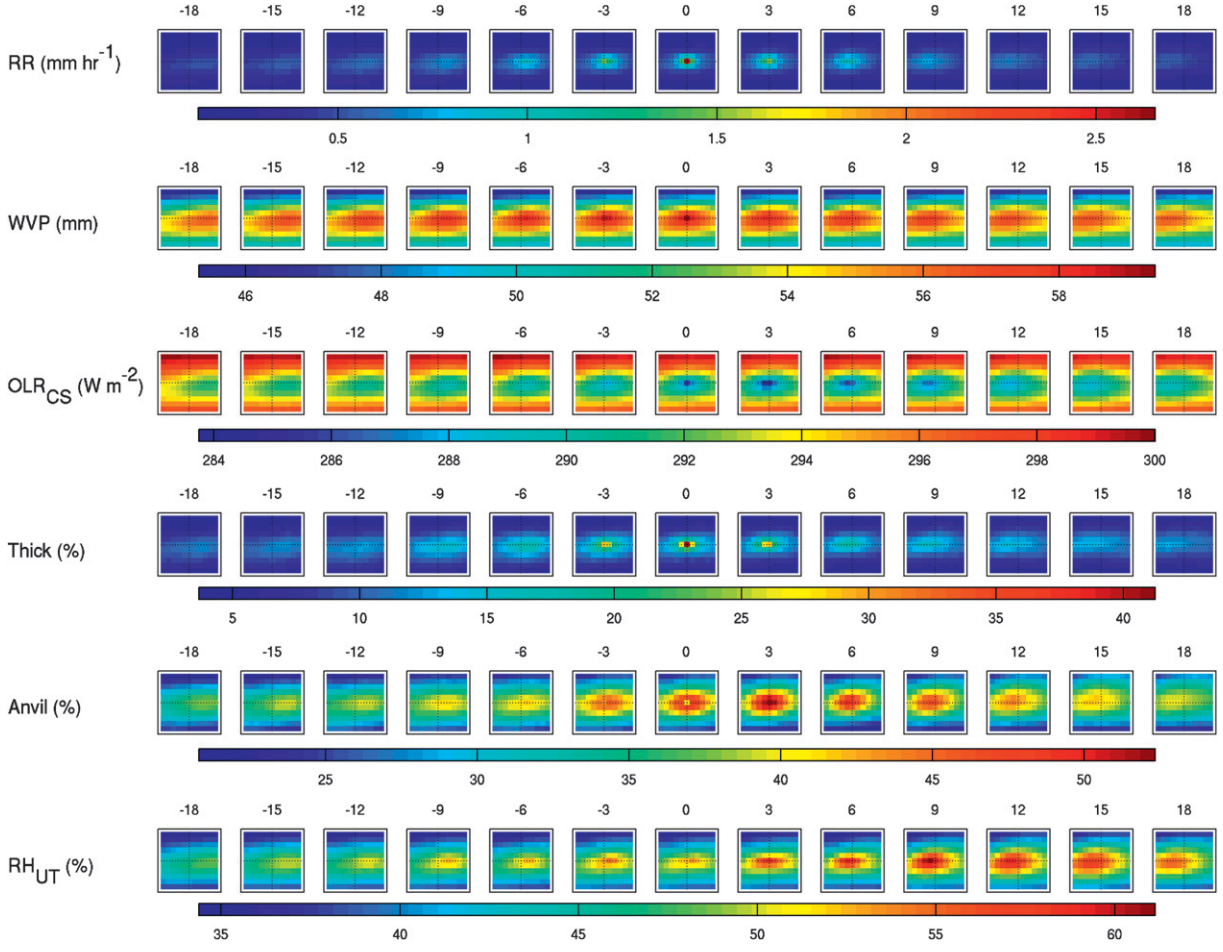

FIG. 1. Plan views of composite mean RR; WVP; OLR_{CS}; high-thick and anvil cloud fractions; and RH_{UT}. Note that the color scale varies among the quantities, including the cloud types. Time lags (h, from the time of the deepest convection) are shown at the top of each plan view. Each domain is 11° × 11°, centered on the RR grid space exceeding the 90th percentile of RR at hour 0, as described in the text.

technique, the central grid space in the plan view at hour 0 contains the maximum RR, and the composite-averaged RR is significantly lower in the hours preceding and following this time. High RRs are confined to the central portion of the domain and are observed for only a few hours before and after peak RR.

Composite mean WVP is highest near the center of the domain, with larger meridional than zonal gradients (i.e., the moist region is elongated in the east–west direction). The zonal elongation of the mean WVP reflects the underlying SSTs in the analysis region, which extends from the northern edge of the western Pacific warm pool in the west to a narrow warm tongue of relatively high SSTs in the east (cf. Fig. 1 of Kubar et al. 2007).

OLR_{CS} is correspondingly lower where the composite mean WVP is higher (i.e., near the center of the domain), because the bulk of the radiation escaping to space originates from a higher altitude, and therefore a lower temperature, where it is more moist. A subtle but important difference between the OLR_{CS} and WVP will become apparent in the anomaly patterns discussed below.

Composite mean high-thick cloud fraction looks nearly identical to the precipitation, maximizing at hour 0 and falling off rapidly away from hour 0, in addition to remaining confined to the center of the domain. This strengthens our confidence that the optical depth threshold chosen to define thick, high clouds ($\tau \geq 32$) is indeed capturing the deep convective cores.

Whereas the high-thick clouds only cover the heavily precipitating region and peak in phase with the precipitation, the anvil cloud fractions cover a larger area of the domain and peak at hour +3. The spatial patterns and evolution of the anvil cloud fraction lends credence to our choice of optical depth ranges defining anvil clouds: We expect greater spatial coverage of anvils relative to deep convective cores, as well as a time lag between peak convection and their maximum extent,

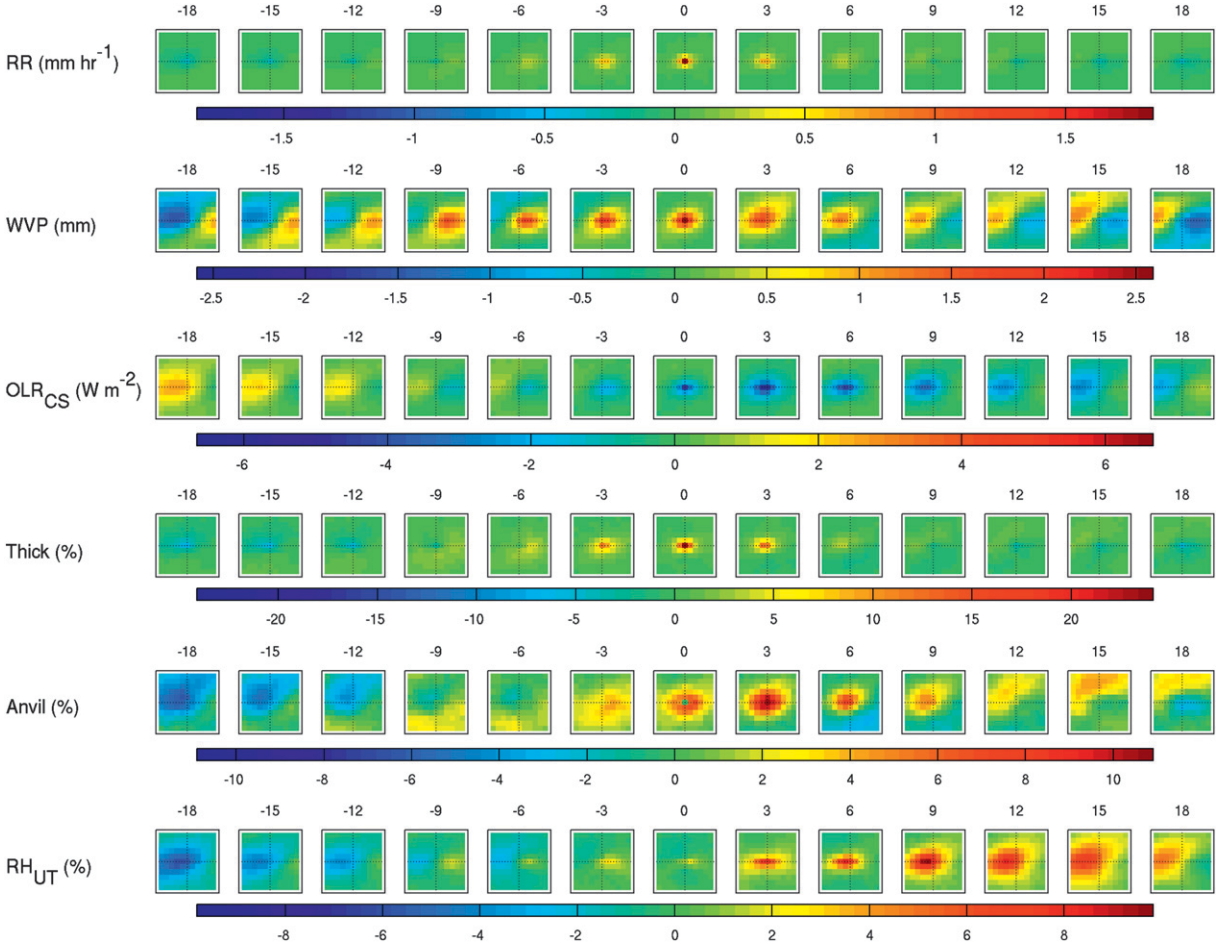

FIG. 2. Same as Fig. 1, but for the anomalies from the composite mean. Note that the anomalies are calculated with respect to the temporal mean of the composite mean pattern over the entire 48-h period, though only a 36-h subset is shown.

because they spread outward from deep convection. This result is also consistent with previous studies (Soden 2000, 2004; Tian et al. 2004; Horvath and Soden 2008) that show a time lag between the peak convective cloud fraction and the peak anvil cloud fraction.

High-thin cloud is well distributed in space and time outside of where the high-thick and anvil clouds are predominant (not shown). The largest high-thin cloud fractions tend to be near the edge of the anvil clouds.

To present the evolution of the response to precipitation events more clearly, Fig. 2 shows plan views of the anomalies that are calculated by subtracting the temporal mean of the composite mean pattern over the 48-h period from each time lag. In addition, fractional coverage and anomaly magnitudes of these fields are plotted in Fig. 3. Fractional coverage of the anomaly refers to the fraction of the 11° × 11° domain that is occupied by grid spaces that are greater than or equal to e^{-1} of the maximum anomaly observed over the entire composite period. The magnitude of the anomaly is defined as the maximum anomaly at each time lag. In the case of $\mathrm{OLR_{CS}}$ and ω_{UT}, computations are done with respect to the largest negative anomaly at each time lag. We choose these metrics rather than simply taking spatial averages across the domain because they retain scale and magnitude information, allowing for the separation of small-scale but very anomalous features from large-scale, weakly anomalous features, which might appear as identical in spatial averages. For anomalies that are three-dimensional (e.g., RH anomalies), we first average the composite anomalies over the appropriate levels (e.g., between 500 and 200 hPa for upper-tropospheric anomalies), and then calculate the fractional coverage such that we are only reporting the horizontal extent of the anomalies. Error bars represent the 95% confidence limits averaged in space over the domain.

RR anomalies (Fig. 2) look identical to composite mean RRs (Fig. 1) because we have isolated very

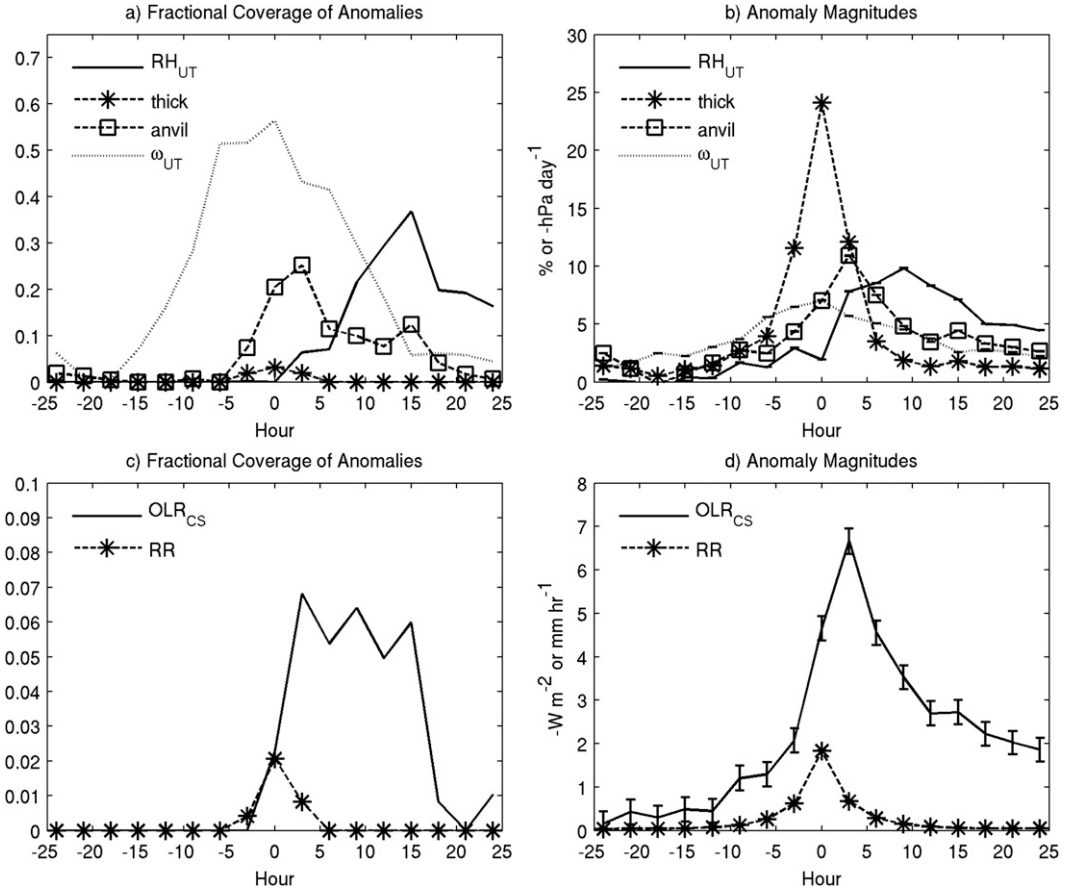

FIG. 3. (left) Fractional coverage and (right) magnitude of (top) RH_{UT}; high-thick and anvil cloud fraction; and ω_{UT}; and (bottom) OLR_{CS} and RR anomalies. Note that the amplitudes of ω_{UT} and OLR_{CS} anomalies are plotted with reversed sign for the purposes of comparison, and that the y axes are different in each panel. Error bars represent the 95% confidence intervals.

extreme RR events. Anomalously high RRs are confined to the central portion of the domain and peak at approximately 2 mm h^{-1} at hour 0.

Peak WVP anomalies coincide with the peak RR, which is consistent with the instantaneous correlations between RR and WVP shown in Bretherton et al. (2004). Anomalies of WVP clearly show a westward propagation of a moist signature, though the fractional coverage of the WVP anomaly remains relatively constant as the system crosses the domain. Thus, it is likely that the majority of the convection observed in these composites does not occur spontaneously, but rather is organized into convective systems that propagate from east to west in time, as documented by Reed and Recker (1971).

As alluded to above, OLR_{CS} anomalies behave quite differently from WVP anomalies. Rather than peaking at hour 0, they reach maximum amplitude following the convection and are anomalously lower in the 24 h following convection than in the 24 h prior to convection (Fig. 3d). As will be shown below, the region of reduced OLR_{CS} corresponds to a sustained moist anomaly in the upper troposphere following deep convection.

Whereas anomalously high-thick cloud fractions only cover the heavily precipitating region and peak in phase with the precipitation, the anvil cloud fraction anomalies cover a larger area of the domain, peak at hour +3, and remain extensive for several hours following convection (Figs. 3a,b). The 3-h lag in peak anvil cloud coverage is roughly consistent with the results of Tian et al. (2004), who show that high clouds observed from geostationary satellites lag deep convection by 3–9 h, and Horvath and Soden (2008), who show that maximum cirrus anvil cloud cover occurs 4–5 h after peak convection. (Recall that a lag of +3 encompasses cloud observations that occurred between 1.5 and 4.5 h after peak RR.)

The region occupied by anomalously large fractions of high-thin cloud (not shown) is larger at nearly all times than either high-thick or anvil cloud, though the anomalies themselves are quite small (~2%). This

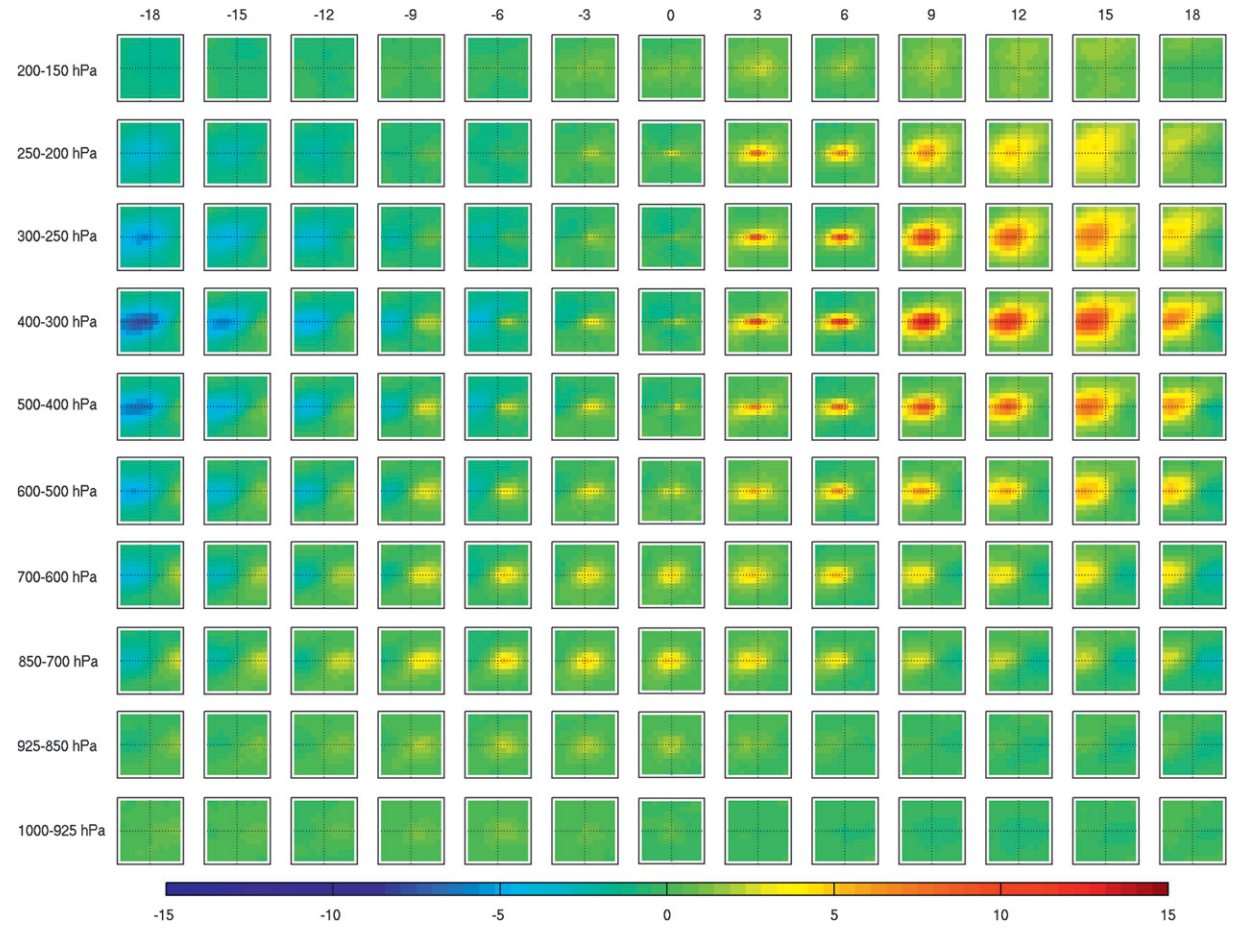

FIG. 4. Plan views of anomalies of RH (%), plotted as a function of pressure between 1000 and 150 hPa. Each domain is 11° × 11°, centered on a RR grid space exceeding the 90th percentile of RR at hour 0, as described in the text. Note that the anomalies are calculated with respect to the temporal mean of the composite mean pattern over the entire 48-h period, though only a 36-h subset is shown.

difference would be more dramatic if the fractional coverage was calculated over a larger domain that captures the broad horizontal extent of high-thin cirrus clouds.

The asymmetry in OLR_{CS} anomalies in the presence of symmetric WVP anomalies can be explained by the pattern of RH anomalies, shown in Fig. 4. Whereas the low-level (below 700 hPa) RH anomalies peak just prior to the maximum RR (hour 0), the upper troposphere (600–200 hPa) is anomalously moist between 3 and 24 h following the convection in both regions. The upper-tropospheric RH (RH_{UT}) anomalies are much larger than the lower-tropospheric RH (RH_{LT}) anomalies, and peak around 10% at hour +9 (Fig. 3b). Anomalies above 200 hPa are negligible. Peak-to-peak anomalies in RH_{UT} of approximately 30% (a roughly 15% amplitude variation about a 50% composite mean state) can be contrasted with the peak-to-peak variations in WVP of approximately 10% (a roughly 5-mm-amplitude variation about a 50-mm composite mean state) over the course of the composite. These differences underscore how small variations in column water vapor may be associated with much larger variations in relative humidity at the very dry upper levels.

These results are consistent with the lag correlations between radar-derived rain rate and lower- and upper-tropospheric RH from radiosondes shown in Sobel et al. (2004): RH_{LT} is highly correlated with rain rate at lags of −6 and 0 h, while the peak correlation between RH_{UT} and rain rate occurs at a lag of +6 h. The peak correlation is stronger for RH_{UT} than for RH_{LT}.

The fractional coverage of the RH_{UT} anomaly region increases until at least hour +15 (Fig. 3a). Beyond hour +18, the RR anomaly has moved out of the domain, but the residual RH_{UT} anomaly near the western edge of the domain is still greater than that at the center of the domain at hour 0. It is unlikely that the moist signature

is an artifact of increased exposure of clear, humid sky because the anvil cloud thins and dissipates. The RH_{UT} anomaly is not confined to regions on the edges of the anvil cloud, but rather monotonically spreads outward from the center of the domain for 15 h following peak RR, while the anvil cloud coverage grows until hour +3 and decays thereafter. It is plausible, however, that the moistening mechanism posited by Sherwood (1999) is operating, in which radiative heating within the thinning anvil cloud is causing diabatic ascent, thereby moistening the upper levels. Moistening by this process and by sublimation of cloud ice and hydrometeors are likely secondary to moistening that is due to horizontal advection away from the site of deep convection, as shown in Salathé and Hartmann (1997), Pierrehumbert and Roca (1998), Dessler and Sherwood (2000), Luo and Rossow (2004), and John and Soden (2006) .

It is important to note that fractional anomalies from the composite mean mixing ratio (not shown) exhibit the same patterns and magnitudes as the RH anomalies, indicating that the positive RH anomalies at upper levels are not due to temperature changes. The temperature perturbations (not shown) are negligible (on the order of 0.1 K throughout the troposphere), and changes in RH are almost entirely due to mixing ratio changes. Previous analysis has noted the absence of substantial temperature perturbations over the course of several individual convective events (Sobel et al. 2004) and over the course of a composite easterly wave (Reed and Recker 1971).

To elucidate the coevolution of humidity and vertical motion, spatial averages of omega and anomalies of omega and RH across the 11° × 11° domain are calculated (Fig. 5). Although upward motion is observed throughout the troposphere at all times in the composite period, it shifts from being bottom heavy prior to convection to being top heavy following the convection. Anomalous upward motion reaches peak amplitude in the upper troposphere at hour 0 (Fig. 3b), but occupies the deepest region of the troposphere at hour −3 (Fig. 5). The lower troposphere is anomalously subsiding (i.e., domain-averaged ascent in the lower troposphere is weaker) at hour 0, indicating the presence of convective and mesoscale downdrafts associated with the heavy rain (Fig. 5). Both the fractional coverage and the magnitude of the upper-tropospheric vertical motion (ω_{UT}) anomaly reach a broad peak around hour 0 (Figs. 3a,b).

Rough calculations show that the magnitude of spatial mean composite ω anomaly is consistent with the spatial mean composite RR anomaly. Consider anomalies from the steady-state column water vapor budget for a typical marine deep convective region in the tropics. The dominant balance is between precipitation and column-integrated vertical moisture transport, with evaporation and column-integrated horizontal moisture convergence being secondary. Assuming a tropospheric mean value of omega that is half as large as its mid-troposphere maximum, and a boundary layer mixing ratio of 20 g kg^{-1}, this relationship predicts that a 1 mm day^{-1} precipitation anomaly, which is on the order of spatially averaged RR anomalies observed in this study, corresponds to a ω anomaly of −10 hPa day^{-1}. Indeed, we observe spatially averaged ω anomalies that are approximately this magnitude, which indicates that the reanalysis is (roughly) capturing the vertical motion associated with deep convection.

Further consistency is evident between the evolution of the spatially averaged vertical motion anomalies and the spatially averaged humidity anomalies shown in Fig. 5c. Spatially averaged RH anomalies clearly show a moist anomaly prior to peak convection at the low levels (below 700 hPa), followed by a significantly larger moist anomaly at upper levels after the peak convection. Roughly, moistening occurs where there is anomalous ascent (e.g., in the lower troposphere between hours −21 and −3 and in the upper troposphere between hours −12 and +12), and drying occurs where there is anomalous descent (e.g., in the upper troposphere between hours −24 and −18 and between hours +15 and +24). This is to be expected, given that the humidity tendency is proportional to the magnitude of upward motion in the presence of a large vertical gradient of absolute humidity.

The vertical motions provided on the 2.5° × 2.5° reanalysis grids are unlikely to capture all of the small-scale motions that characterize either deep convection or motions driven by local cloud radiative effects, and are largely model output rather than observations in the remote areas of the tropical Pacific studied here. Nonetheless, the reanalysis does a remarkably good job, at least in the composite sense, of producing a vertical motion field in an environment of tropical deep convection that evolves in a manner that is similar to that shown in observational studies (e.g., Fig. 8 of Reed and Recker 1971; Fig. 6 of Gamache and Houze 1983; Fig. 8f of Nuret and Chong 1998) and that is consistent with humidity and precipitation anomalies observed from space.

b. Composites as a function of spatially averaged RR

We now sort the composites by the spatially averaged RR at hour 0. While still requiring that the central RR grid space at hour 0 in each composite exceeds the 90th percentile, the composites are now stratified by the average RR over the entire domain. This separates large systems with heavy precipitation occurring over broad regions from small systems that are more confined in

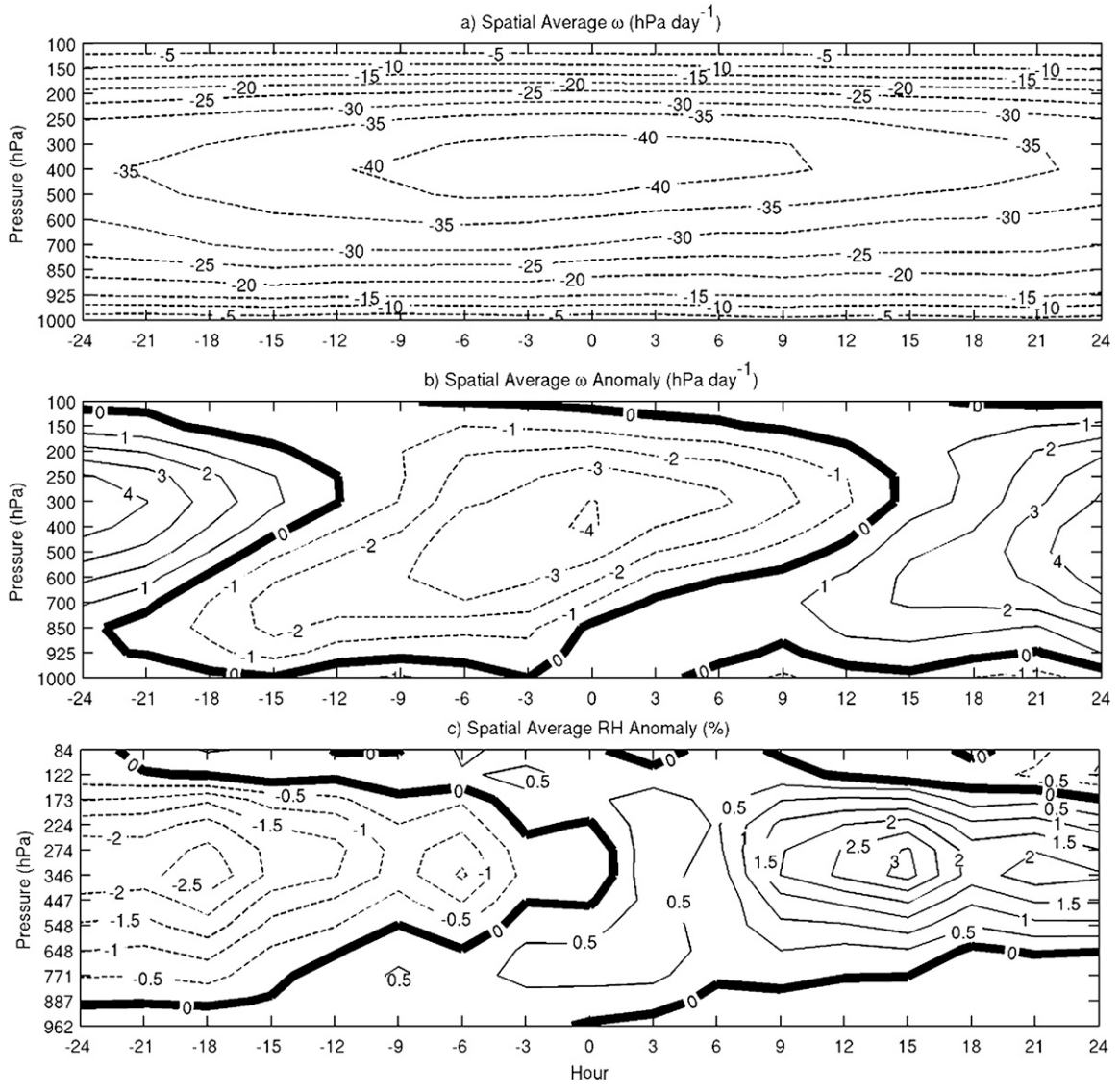

FIG. 5. Spatial averages over the 11° × 11° domain of (a) composite mean ω, (b) ω anomalies, and (c) RH anomalies. The thick solid line is the zero contour.

space. For consistency, the anomaly regions are calculated with respect to the maximum anomalies observed using all observations (i.e., the maxima from the unsorted results discussed above rather than the maxima within each RR regime). Figures 6 and 7 show fractional coverage and the magnitude of the anomalies of RR, OLR_{CS}, and high, thick and anvil cloud fraction for each RR regime, along with the results using all of the observations (i.e., the unsorted results shown in Fig. 3). In general, the composite anomaly plan views (not shown) have similar patterns to those generated using all of the observations (Figs. 2, 4), but the size and amplitude of the anomalies tends to increase with spatially averaged RR.

Anomalously high RRs cover the greatest fraction of the domain at hour 0 in all regimes, with fractional coverage increasing with spatially averaged RR (Fig. 6a). Because the scale of the convective system increases with RR regime, the anomalous RR region arrives in the domain earlier and exits later with increasing RR regime. The anomaly amplitudes (Fig. 6b) are indistinguishable among RR regimes at hour 0 because the composites are all centered on RRs exceeding the 90th percentile. RR anomaly magnitudes are slightly greater preceding and following hour 0 for higher RR regimes, indicating intense convection occurring over a longer period of time. This tendency for larger systems

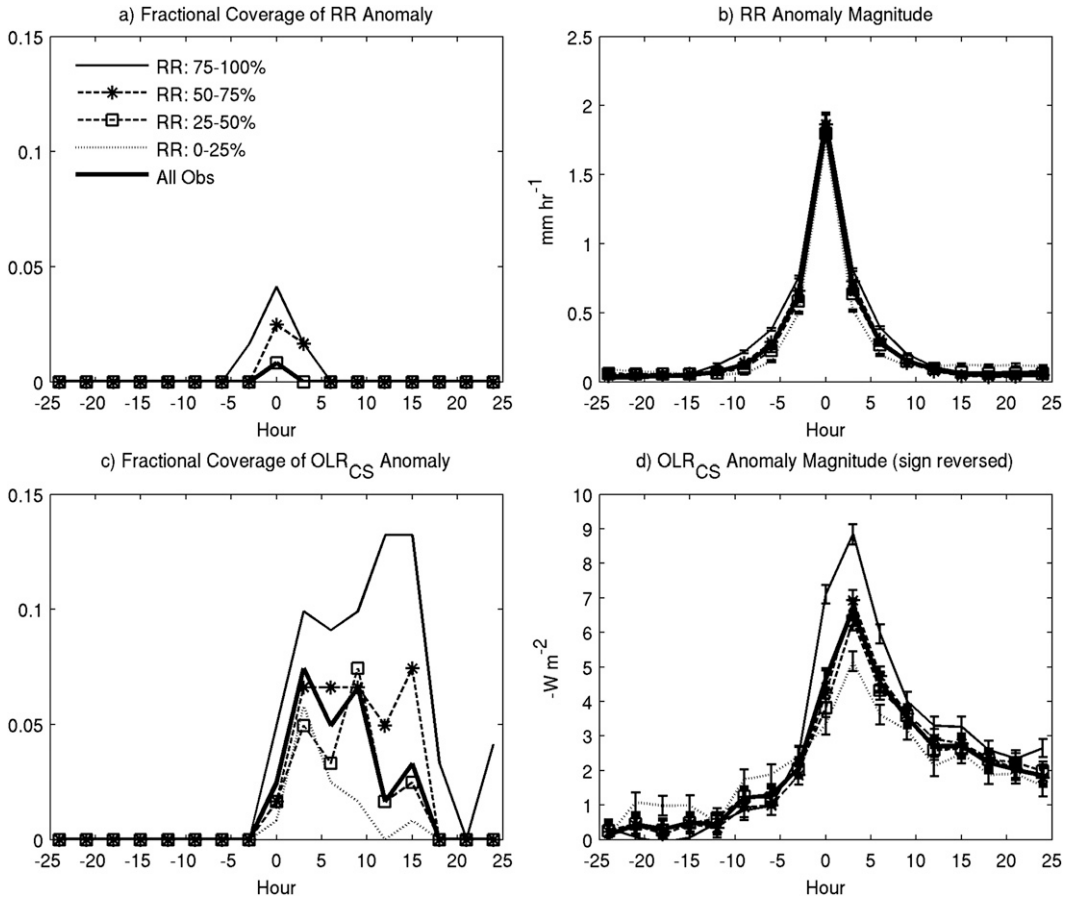

FIG. 6. (a),(c) Fractional coverage and (b),(d) magnitude of (a),(b) RR and (c),(d) OLR_{CS} anomalies for composites in each quartile of spatially averaged RR. The thick, solid line shows the fractional coverage and amplitude of these quantities for all composites centered on RRs exceeding the 90th percentile. Error bars represent the 95% confidence intervals. Note that the sign of the OLR_{CS} anomaly magnitude is reversed for the purposes of comparison and that only (a) and (c) have the same *y*-axis limits.

to have longer lifetimes is also noted in Futyan and Del Genio (2007). Thus, sorting by spatially averaged RR at hour 0 tends to separate large, longer-lived systems (top quartile) from small, shorter-lived systems (bottom quartile).

Though the WVP anomaly peaks at hour 0 in all regimes, the anomaly amplitude is larger in the lower RR regimes (not shown). This is consistent with the relationship between instantaneous RR and absolute WVP derived in Bretherton et al. (2004). An implication of the relationship is that a larger WVP anomaly is required in a relatively dry environment (lower RR regime), compared to a relatively moist environment (higher RR regime), to produce the same RR anomaly, as is the case here. Again, the symmetry of WVP anomaly amplitude about hour 0 can be contrasted with the OLR_{CS} anomaly (Fig. 6d).

The fractional coverage of the OLR_{CS} anomaly increases from just before convection until reaching peak coverage following convection (Fig. 6c). The anomalies are generally greater and more expansive for the high RR regimes and reach maximum size at the same time as the corresponding RH_{UT} anomalies (discussed below). Maximum (absolute) OLR_{CS} anomalies between -5 and -9 W m^{-2} are observed at hour $+3$ in all RR regimes (Fig. 6d), but the fractional coverage tends to remain expansive until at least hour $+12$ in all RR regimes.

The fractional coverage and anomaly magnitude of high, thick cloud fraction evolves in a nearly identical manner to RR anomalies, though the fractional coverage is larger than that of RR (Fig. 7a). Similar to the RR anomalies, high, thick cloud fraction anomalies grow rapidly to a peak at hour 0, and then rapidly decrease (Fig. 7b), with growth and decay being more rapid in the lower RR regimes. The fractional coverage is likewise stratified by spatially averaged RR, with thick cloud occupying a larger portion of the domain throughout the composite period in the higher RR regimes. Plan

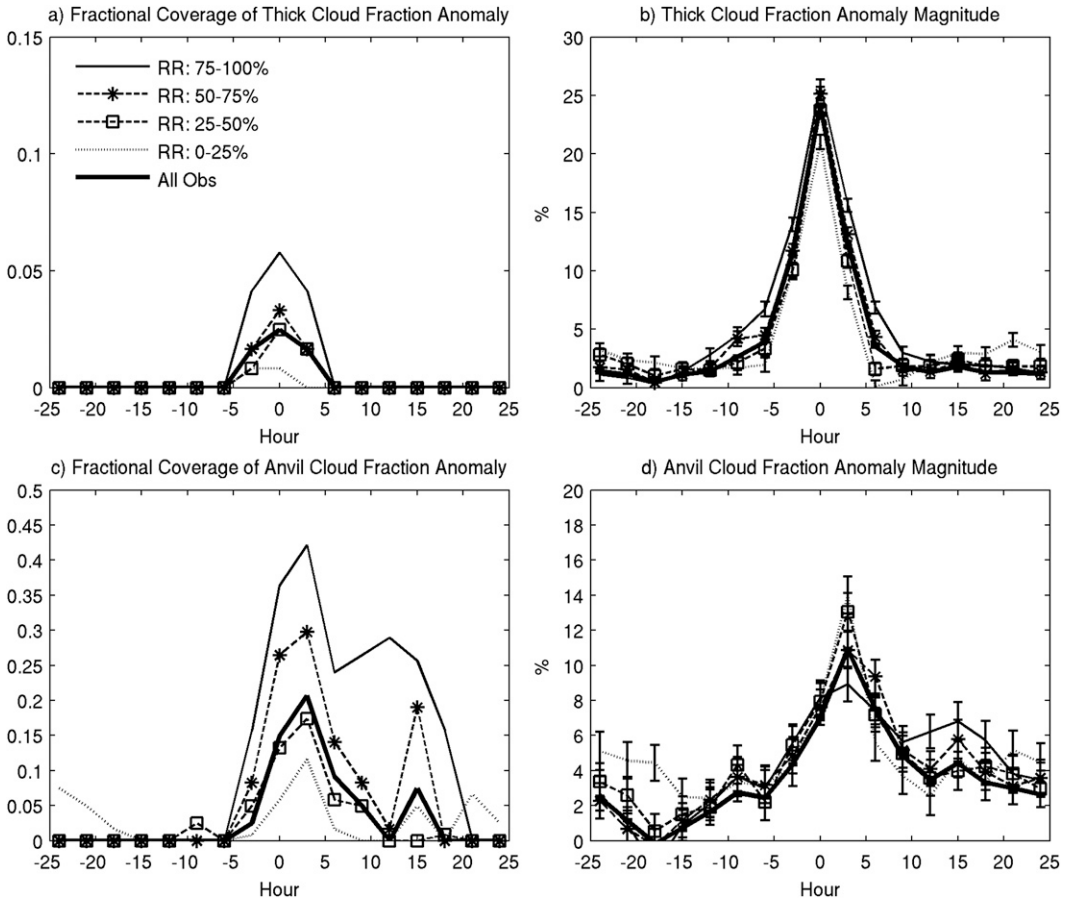

FIG. 7. Same as Fig. 6, but for (a),(b) high-thick and (c),(d) anvil cloud fraction anomalies. Note that the y axes are different in each panel.

views of thick cloud fraction anomalies show that the anomaly region expands zonally and becomes more persistent with more intense RR regime (not shown).

The evolution of anvil cloud fraction anomalies is quite different from those of RR and deep convective cloud. Anomalously high anvil cloud fractions reach their maximum extent and maximum amplitude at hour +3 in all RR regimes (Figs. 7c,d). After hour +3, the anomaly magnitude tends to be slightly greater in the higher RR regimes. The fraction of the domain covered by the anomalously large anvil cloud fractions is greater for larger RR regimes at all times in the composite. Thus, deep convection that occupies a larger area of the domain results in broader anvil cloud coverage, though peak coverage consistently occurs at hour +3 across the regimes.

Because of the spatial and temporal ubiquity of high, thin clouds throughout the composite period and throughout the composite domain, high, thin cloud fraction anomalies are small and changes in their fractional coverage largely reflect changes in the coverage of high, thick and anvil cloud fractions (not shown).

Profiles of RH anomalies averaged over the $11° \times 11°$ domain between hours 0 and +24 are shown in Fig. 8. It is clear that the magnitude of the moistening resulting from convection increases with RR regime. In the top three RR regimes, peak moistening occurs in the upper troposphere, but the lowest RR regime exhibits moistening in the low to midtroposphere. This indicates that the magnitude and vertical location of moistening increases with spatially averaged RR such that broader precipitation systems exhibit greater moistening as well as an elevated region at which the moistening occurs. As Futyan and Del Genio (2007) show, the population of convective systems is dominated by smaller systems with maximum radii less than 300 km. The prevalence of such systems, which appear to detrain at lower levels than their large-scale counterparts, may explain the observation that moisture fluctuations are greatest in the midtroposphere (Allan et al. 1999; Sinha and Harries 1997). However, Futyan and Del Genio (2007) do not observe any correlation between the system size (area covered by brightness temperatures less than 238 K) and

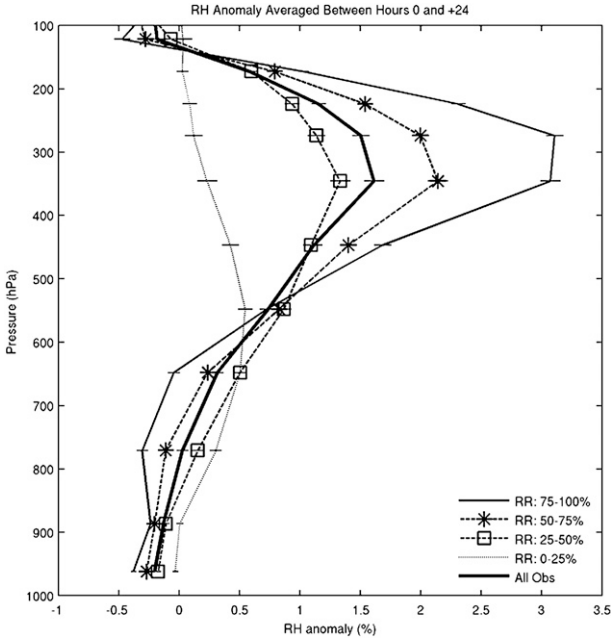

FIG. 8. RH anomalies averaged over the 11° × 11° domain between hours 0 and +24 for composites in each quartile of spatially averaged RR.

convective storm height (minimum brightness temperature reached over its lifetime).

Figure 9 shows the fractional coverage and magnitude of anomalies of RH_{UT} and ω_{UT} for each RR regime, along with the results using all of the observations. Between hours 0 and 6, the fractional coverage of the RH_{UT} anomalies in the four regimes is virtually indistinguishable (Fig. 9a). Between hours +6 and +15, the moist anomaly in the low RR regime tends to maintain its size, covering approximately 10% of the domain, while the anomalies in the other regimes continue to spread until at least hour +15. Anomaly size increases with spatially averaged RR, with the second, third, and fourth RR quartiles having RH_{UT} anomalies that occupy approximately 25%, 50%, and 70% of the domain, respectively, at their peak extents. The region of anomalously high RH_{UT} remains extensive for the remainder of the composite period in all regimes. Clearly, deep convection is pumping moisture into the upper troposphere over a larger scale in the higher RR regimes throughout the composite period. In the lower RR regimes, the convection is occurring on a smaller scale, and so the moistening is confined to the center of the domain (not shown).

The RH_{UT} anomaly amplitudes peak at hour +9 in the lowest three RR quartiles and at hour +12 in the top RR quartile (Fig. 9b). After hour +9, the RH_{UT} anomalies are clearly stratified by the RR regime, with larger anomalies in higher RR regimes. Thus, both the size and amplitude of moist anomalies increase with the size and amplitude of convection. It is important to recall that the anomalies are calculated individually for each regime with respect to the mean over their respective composite periods. Both the composite mean RH_{UT} (not shown) and the maximum RH_{UT} anomaly are greater in the higher RR regimes than the lower RR regimes. It is interesting to note that RH_{UT} anomalies always peak several hours after the peak anvil extent.

The ω_{UT} anomalies (Fig. 9c,d) are likewise stratified by the RR regime, with high RR regimes characterized by largest ω_{UT} anomalies (in both extent and magnitude). The ω anomalies in the low RR regime are essentially zero throughout the depth of the troposphere, indicating that the reanalysis is not capturing the updrafts that characterize deep convection on scales smaller than about 250 km (the resolution of the reanalysis). The spatial extent of ω_{UT} anomalies in the top three RR regimes exhibits a broad peak between hours −9 and +9 and increases with the RR regime. In all but the lowest RR regime, the anomalous ascent covers a large portion of the domain between hours −12 and +12. Upper-tropospheric ascent peaks at hour 0 in the top three RR regimes. It should also be noted that the top three RR regimes show evidence of an upward-propagating ω anomaly over the composite period (not shown).

5. Conclusions

In addition to its importance for the tropical mean circulation, deep convection is the main mechanism for vertically redistributing clouds and humidity throughout the tropics. This latter virtue is of critical importance for the energy balance of the entire planet, and serves as a fundamental link between discrete mesoscale atmospheric processes and the earth's climate. Making observations of these small-scale processes in great detail in a range of locations is absolutely necessary for better understanding the earth's climate and using this information to model climate change.

The analysis herein has illustrated a means of studying the complex interactions of precipitation, clouds, humidity, radiation, and dynamics at relatively fine spatial and temporal scales, and can be extended over the entire globe. A compositing technique centered in space and time on locations in the Pacific ITCZ experiencing intense precipitation was used to investigate the response of clouds, humidity, clear-sky OLR, and vertical motion to tropical deep convection. Nearly 60% of the total precipitation in the tropical Pacific falls in events upon which these composites are based. The results that are shown are consistent throughout the convective tropics

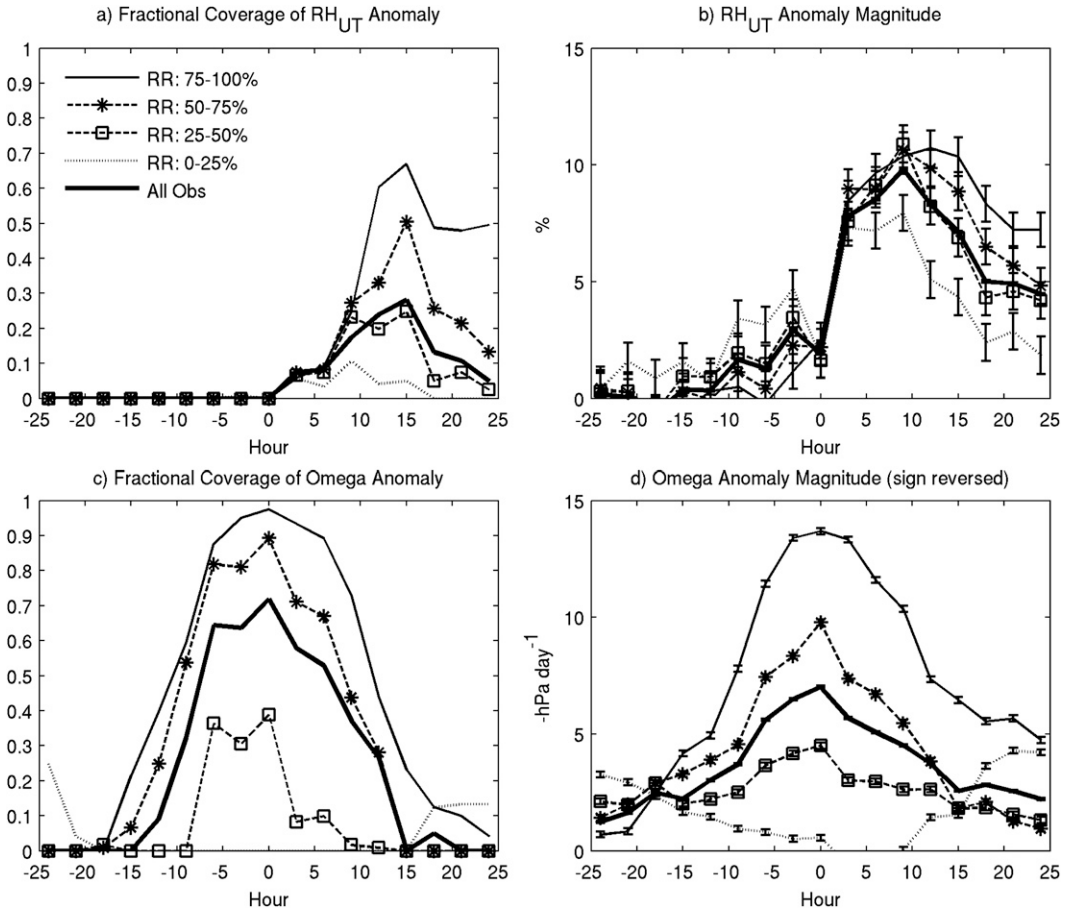

FIG. 9. Same as Fig. 6, but for (top) RH_{UT} and (bottom) ω_{UT} anomalies. Note that the sign of the ω_{UT} anomaly magnitude is reversed for the purposes of comparison.

for all seasons, regardless of whether the observations come from the ascending or descending *Aqua* orbit.

Moistening occurs at low levels prior to convection and in the upper troposphere for several hours following convection. The magnitude of the RH anomaly at upper levels is much greater than that at low levels, and spreads outward for at least 15 h to cover a much larger region than that occupied by the precipitation anomaly. Though variations in domain-averaged WVP are on the order of 10% over the composite period and peak with the precipitation event, the RH_{UT} variations are of the order of 30% and significantly lag the precipitation event. This demonstrates that convection removes water vapor from a very moist source (boundary layer) by condensing a portion into precipitation and by transporting a portion to the very dry upper troposphere, resulting in dramatic changes to the upper-level moisture. WVP is dominated by the contribution from the boundary layer moisture; thus, regions with large values of column water vapor are favored sites for deep convection to ventilate the boundary layer and moisten the upper troposphere. Because of the upper troposphere's strong leverage on IR emission to space, these moisture perturbations at upper levels cause OLR_{CS} to be significantly lower following convection.

Whereas thick convective cloud fractions peak at the time of the intense precipitation event, anvil clouds spread outward from the convective region in time, reaching maximum spatial extent 3 h later. Large-scale vertical motion is upward throughout the troposphere during the composite period, but anomalous ascent shifts from the lower troposphere to the upper troposphere over the course of the convection. This transition from bottom- to top-heavy ascent is consistent with previous observational studies of tropical convection and corresponds well with the pattern of moistening observed here. It is also impressive that the reanalysis can capture the detailed structure and evolution of vertical motion associated with independently measured deep convective events.

Broader regions of anomalously high RRs tend to be associated with larger anvil cloud fraction, OLR_{CS},

RH_{UT}, and ω_{UT} anomalies, as is shown by sorting the composites by the spatially averaged RR at the time of peak convection. Whereas convective moistening peaks in the upper troposphere in the top three RR regimes, moistening is confined to lower levels in the lowest RR regime, indicating reduced detrainment height for very small-scale systems. The temporal evolution of the anomalies is consistent across all spatial scales of intense convection, however.

Tropical convection is organized on a broad range of spatiotemporal scales. An interesting extension of the analysis presented in this work would be to investigate the similarity of the results shown here to those at larger spatial and longer temporal scales. For example, does the persistence in upper-tropospheric humidity anomalies following precipitation anomalies also exist at larger spatial and temporal scales? If so, how does this shape our understanding of tropical deep convection and its role in climate, and what can this tell us about interactions at various scales?

Acknowledgments. The work presented in this paper was supported by a NASA Earth and Space Science Fellowship and NASA EOS Grant NNG05GA19G. We thank Chris Bretherton, Rob Wood, and Qiang Fu as well as two anonymous reviewers for their helpful comments and suggestions on this work. AIRS data are distributed by the AIRS Data Services branch of the Goddard Earth Sciences Distributed Active Archive Center (DAAC), Goddard Space Flight Center (GSFC), Greenbelt, Maryland. MODIS data are distributed by the level 1 and Atmosphere Archive and Distribution System, GSFC, Greenbelt Maryland. AMSR-E data are provided by Remote Sensing Systems and sponsored by the NASA Earth Science REASoN DISCOVER Project and the AMSR-E Science Team. TMPA data are distributed by the Goddard Earth Sciences DAAC, GSCF, Greenbelt, Maryland. NCEP–NCAR reanalysis data are provided by the NOAA/OAR/ESRL PSD, Boulder, Colorado.

REFERENCES

Allan, R. P., K. P. Shine, A. Slingo, and J. A. Pamment, 1999: The dependence of clear-sky outgoing longwave radiation on surface temperature and relative humidity. *Quart. J. Roy. Meteor. Soc.,* **125,** 2103–2126.

Aumann, H. H., and Coauthors, 2003: AIRS/AMSU/HSB on the Aqua mission: Design, science objectives, data products, and processing systems. *IEEE Trans. Geosci. Remote Sens.,* **41,** 253–264.

Bretherton, C. S., M. E. Peters, and L. E. Back, 2004: Relationships between water vapor path and precipitation over the tropical oceans. *J. Climate,* **17,** 1517–1528.

Buck, A. L., 1981: New equations for computing vapor pressure and enhancement factor. *J. Appl. Meteor.,* **20,** 1527–1532.

Chen, S. S., and R. A. Houze Jr., 1997: Diurnal variation and life cycle of deep convective systems over the tropical Pacific warm pool. *Quart. J. Roy. Meteor. Soc.,* **123,** 357–388.

Colman, R. A., 2001: On the vertical extent of atmospheric feedbacks. *Climate Dyn.,* **17,** 391–405.

Derber, J. C., D. F. Parrish, and S. J. Lord, 1991: The new global operational analysis system at the National Meteorological Center. *Wea. Forecasting,* **6,** 538–547.

Dessler, A. E., and S. C. Sherwood, 2000: Simulations of tropical upper tropospheric humidity. *J. Geophys. Res.,* **105,** 20 155–20 163.

Fetzer, E. J., A. Elderling, E. F. Fishbein, T. Hearty, W. F. Irion, and B. Kahn, 2005: Validation of AIRS/AMSU/HSB core products for data release version 4.0. NASA Validation Rep. JPL D-31448, 60 pp. [Available online at http://disc.gsfc.nasa.gov/AIRS/documentation/v4_docs/V4.0_Validation_Report.pdf/view.]

Futyan, J. M., and A. D. Del Genio, 2007: Deep convective system evolution over Africa and the tropical Atlantic. *J. Climate,* **20,** 5041–5060.

Gamache, J. F., and R. A. Houze Jr., 1983: Water budget of a mesoscale convective system in the tropics. *J. Atmos. Sci.,* **40,** 1835–1850.

Gautier, C., Y. Shiren, and M. D. Hofstadter, 2003: AIRS Vis/Near IR instrument. *IEEE Trans. Geosci. Remote Sens.,* **41,** 330–342.

Gettelman, A., E. J. Fetzer, A. Eldering, and F. W. Irion, 2006: The global distribution of supersaturation in the upper troposphere from the Atmospheric Infrared Sounder. *J. Climate,* **19,** 6089–6103.

Hartmann, D. L., L. A. Moy, and Q. Fu, 2001: Tropical convection and the energy balance at the top of the atmosphere. *J. Climate,* **14,** 4495–4511.

Held, I. M., and B. J. Soden, 2000: Water vapor feedback and global warming. *Annu. Rev. Energy Environ.,* **25,** 441–475.

Horvath, A., and B. J. Soden, 2008: Lagrangian diagnostics of tropical deep convection and its effect upon upper-tropospheric humidity. *J. Climate,* **21,** 1013–1028.

Houze, R. A., Jr., 1982: Cloud clusters and large-scale vertical motions in the tropics. *J. Meteor. Soc. Japan,* **60,** 396–410.

——, and A. K. Betts, 1981: Convection in GATE. *Rev. Geophys. Space Phys.,* **19,** 541–576.

Huffman, G. J., and Coauthors, 2007: The TRMM Multisatellite Precipitation Analysis (TMPA): Quasi-global, multiyear, combined sensor precipitation estimates at fine scales. *J. Hydrometeor.,* **8,** 38–55.

Japan Aerospace Exploration Agency, 2005: AMSR-E data users handbook. 3rd ed. JAXA Rep., 105 pp.

John, V. O., and B. J. Soden, 2006: Does convectively-detrained cloud ice enhance water vapor feedback? *Geophys. Res. Lett.,* **33,** L20701, doi:10.1029/2006GL027260.

Kalnay, E., and Coauthors, 1996: The NCEP/NCAR 40-Year Reanalysis Project. *Bull. Amer. Meteor. Soc.,* **77,** 437–471.

Kubar, T. L., D. L. Hartmann, and R. Wood, 2007: Radiative and convective driving of tropical high clouds. *J. Climate,* **20,** 5510–5526.

Luo, Z., and W. B. Rossow, 2004: Characterizing tropical cirrus life cycle, evolution, and interaction with upper-tropospheric water vapor using Lagrangian trajectory analysis of satellite observations. *J. Climate,* **17,** 4541–4563.

Nuret, M., and M. Chong, 1998: Characteristics of heat and moisture budgets of a mesoscale convective system observed

during TOGA-COARE. *Quart. J. Roy. Meteor. Soc.,* **124,** 1163–1181.

Pierrehumbert, R. T., 1995: Thermostats, radiator fins, and the local runaway greenhouse. *J. Atmos. Sci.,* **52,** 1784–1806.

——, and R. Roca, 1998: Evidence for control of Atlantic subtropical humidity by large-scale advection. *Geophys. Res. Lett.,* **25,** 4537–4540.

Platnick, S., M. D. King, S. A. Ackerman, W. P. Menzel, B. A. Baum, J. C. Riedi, and R. A. Frey, 2003: The MODIS cloud products: Algorithms and examples from TERRA. *IEEE Trans. Geosci. Remote Sens.,* **41,** 459–473.

Reed, R. J., and E. E. Recker, 1971: Structure and properties of synoptic-scale wave disturbances in the equatorial Western Pacific. *J. Atmos. Sci.,* **28,** 1117–1133.

Salathé, E. P., and D. L. Hartmann, 1997: A trajectory analysis of tropical upper-tropospheric moisture and convection. *J. Climate,* **10,** 2533–2547.

Sherwood, S. C., 1999: On the moistening of the tropical tropopause by cirrus clouds. *J. Geophys. Res.,* **104,** 11 949–11 960.

——, and R. Wahrlich, 1999: Observed evolution of tropical deep convective events and their environment. *Mon. Wea. Rev.,* **127,** 1777–1795.

Shine, K. P., and A. Sinha, 1991: Sensitivity of the Earth's climate to height-dependent changes in the water vapour mixing ratio. *Nature,* **354,** 382–384.

Sinha, A., and J. E. Harries, 1997: The earth's clear-sky radiation budget and water vapor absorption in the far infrared. *J. Climate,* **10,** 1601–1614.

Sobel, A. D., S. E. Yuter, C. S. Bretherton, and G. N. Kiladis, 2004: Large-scale meteorology and deep convection during TRMM KWAJEX. *Mon. Wea. Rev.,* **132,** 422–444.

Soden, B. J., 1998: Tracking upper tropospheric water vapor radiances: A satellite perspective. *J. Geophys. Res.,* **103,** 17 069–17 081.

——, 2000: The diurnal cycle of convection, clouds, and water vapor in the tropical upper troposphere. *Geophys. Res. Lett.,* **27,** 2173–2176.

——, 2004: The impact of tropical convection and cirrus on upper tropospheric humidity: A Lagrangian analysis of satellite measurements. *Geophys. Res. Lett.,* **31,** L20104, doi:10.1029/2004GL020980.

——, and R. Fu, 1995: A satellite analysis of deep convection, upper-tropospheric humidity, and the greenhouse effect. *J. Climate,* **8,** 2333–2351.

Spencer, R. W., and W. D. Braswell, 1997: How dry is the tropical free troposphere? Implications for global warming theory *Bull. Amer. Meteor. Soc.,* **78,** 1097–1106.

Susskind, J., C. D. Barnet, and J. M. Blaisdell, 2003: Retrieval of atmospheric and surface parameters from AIRS/AMSU/HSB data in the presence of clouds. *IEEE Trans. Geosci. Remote Sens.,* **41,** 390–409.

——, ——,——, L. Iredell, F. Keita, L. Kouvaris, G. Molnar, and M. Chahine, 2006: Accuracy of geophysical parameters derived from Atmospheric Infrared Sounder/Advanced Microwave Sounding Unit as a function of fractional cloud cover. *J. Geophys. Res.,* **111,** D09S17, doi:10.1029/2005JD006272.

Tian, B., B. J. Soden, and X. Wu, 2004: Diurnal cycle of convection, clouds, and water vapor in the tropical upper troposphere: Satellites versus a general circulation model. *J. Geophys. Res.,* **109,** D10101, doi:10.1029/2003JD004117.

Udelhofen, P. M., and D. L. Hartmann, 1995: Influence of tropical cloud systems on the relative humidity in the upper troposphere. *J. Geophys. Res.,* **100** (D4), 7423–7440.

Yanai, M., S. Esbensen, and J.-H. Chu, 1973: Determination of bulk properties of tropical cloud clusters from large-scale heat and moisture budgets. *J. Atmos. Sci.,* **30,** 611–627.